

CrossMark
click for updatesCite this: *J. Mater. Chem. A*, 2017, 5,
4093

Study of ITO-free roll-to-roll compatible polymer solar cells using the one-step doctor blading technique†

Yuanbao Lin,^a Chaosheng Cai,^a Yangdong Zhang,^a Wenhao Zheng,^a Junyu Yang,^a
Ergang Wang^b and Lintao Hou^{*a}

Extremely simple one-step coating ITO-free inverted polymer solar cells (IFIPSCs) have been fabricated using a novel film deposition method—doctor blading technique, which is completely compatible with roll-to-roll (R2R) manufacturing. Delamination of the interfacial buffer layer (IBL) from the photoactive mixtures is achieved *via* a spontaneous vertical self-assembly. The performance of one-step doctor-blading IFIPSCs is primarily influenced by the inherent IBL stratification purity rather than the fine donor/acceptor phase separation for the rigid backbone PTB7 system, which is significantly different from that of the conventional two-step doctor blading devices. The surface energy results strongly demonstrate that the formation of the interfacial layer between the ITO-free cathode and the photoactive layer is significantly controlled by the solvent drying time, which determines the self-assembly quality and can be greatly manipulated from 2700 to 1200 s by different substrate temperatures. It's worth noting that the pure interfacial layer formed at low substrate temperatures improves charge separation and transport, whereas high substrate temperatures limit its growth, leading to the decrease of device performance. The detailed relationship between the self-assembly interfacial layer and the internal resistance and capacitance is revealed by impedance spectroscopy. Encouraging power conversion efficiency (PCE) of 6.56% is achieved from simple one-step doctor-blading ITO-free devices at a very low substrate temperature of 25 °C, which is energy saving and appropriate for industrialized R2R production. In contrast, the highest PCE of 7.11% ever reported for two-step doctor-blading ITO-free IFIPSCs was obtained at a high substrate temperature of 60 °C for achieving a fine morphology without regard to the vertical delamination. Furthermore, for crystalline polymer systems like P3TI with a semi-flexible chain, it requires a higher substrate temperature of 40 °C to mediate the balance of vertical self-assembly stratification of the interfacial buffer layer and photoactive morphology to maximize the device performance.

Received 20th November 2016
Accepted 23rd January 2017

DOI: 10.1039/c6ta10018j

rsc.li/materials-a

Introduction

Polymer solar cells (PSCs), which possess potential advantages in low-cost flexible large-area fabrication *via* roll-to-roll (R2R) coating technology, have been studied widely in recent years.^{1–6} Based on the bulk heterojunction (BHJ) of a blend of conjugated polymers and fullerene derivatives, power conversion efficiency (PCE) of single-junction PSCs over 11% on the laboratory scale has been achieved, which is considered as the lowest

requirement for commercialization.^{7–9} However, almost all of the high-performance devices are processed by a spin coating method, which is totally ill-suited to a large-area R2R process. Another serious problem with the spin-coating technique is that most of the solution is wasted, *i.e.*, only 10% of the solution is utilized.¹⁰ In contrast, the doctor blading method can perfectly solve these problems. PCEs of 10.03% and 8.31% for tandem and single junction devices have been achieved in recent reports.¹¹ However, for these devices indium tin oxide (ITO) is widely used as the transparent electrode, which is expensive and brittle and is unbecoming to the large-area R2R process. Importantly, for conventional devices, the use of an ITO/poly(3,4-ethylenedioxythiophene):poly(styrene sulfonate) (PEDOT:PSS) stack as the electrode reduces the stability of PSCs due to corrosion of the ITO by the acidic PEDOT:PSS material.^{12,13} It had been reported that ITO-free inverted polymer solar cells (IFIPSCs) have great stability when PEDOT:PSS is used as the top transparent anode, whose structure is more compatible

^aSiyuan Laboratory, Guangzhou Key Laboratory of Vacuum Coating Technologies and New Energy Materials, Guangdong Provincial Key Laboratory of Optical Fiber Sensing and Communications, Department of Physics, Jinan University, Guangzhou 510632, PR China. E-mail: thlt@jnu.edu.cn

^bDepartment of Chemistry and Chemical Engineering, Chalmers University of Technology, SE-412 96, Göteborg, Sweden

† Electronic supplementary information (ESI) available. See DOI: 10.1039/c6ta10018j

with R2R manufacturing due to good flexibility and all solution processing.^{14,15} Moreover, although some novel transparent conductive carbon electrodes were used to replace ITO, the last thermal evaporation metal electrodes structure restricts these types of IFIPSCs to be used in R2R printing.¹⁶

In order to simplify the fabrication process without sacrificing device performance, it was confirmed that one-step coating is a useful method that involves an easy spontaneous vertical phase separation of the interfacial layer from active solutions. Peng *et al.* reported a conjugated interfacial polymer *via* a spontaneous vertical separation in nanocomposites by spin coating. It was shown that doping a 3 wt% conjugated polymer poly[(9,9-bis(3'-(*N,N*-dimethylamino)propyl)-2,7-fluorene)-*alt*-2,7-(9,9-dioctylfluorene)] (PFN) into the polymer thieno [3,4-*b*]thiophene/benzo-dithiophene (PTB7):[6,6]-phenyl-C₇₁-butyric acid methyl ester (PC₇₁BM) bulk photoactive layer can lead to a high PCE of 7.14% in ITO-based PSCs due to the self-organization of PFN molecules to the bottom of the PTB7:PC₇₁BM active layer during the spin-coating process.¹⁷ For the R2R compatible doctor blading technique, Xiong *et al.* reported that the longer film drying time for the doctor-blading processed films allows the highly crystalline polymer to form larger crystals, which increase the geminate recombination and result in lower PCE.¹⁸ In truth, the longer drying time provides the doctor blading method with more advantages than spin coating such as the effective stratification of two functional

layers. Zhu *et al.* demonstrated this approach by using a self-organized interfacial layer based on the small-molecule Phen-NaDPO by doctor blading with a PCE of 5.22%.¹⁹ However, there are still some defects in this method such as using expensive and inflexible ITO electrodes, evaporating MoO₃ and silver electrodes which are not compatible with R2R production,

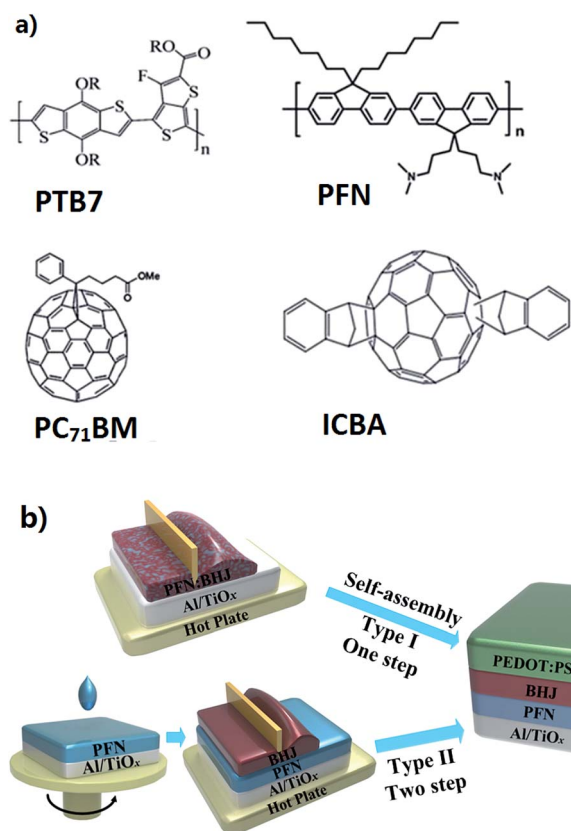


Fig. 1 (a) Molecular structures of PTB7, PFN, PC₇₁BM and ICBA. (b) The doctor-blading fabrication process of Type I and Type II devices with the ITO-free inverted structure.

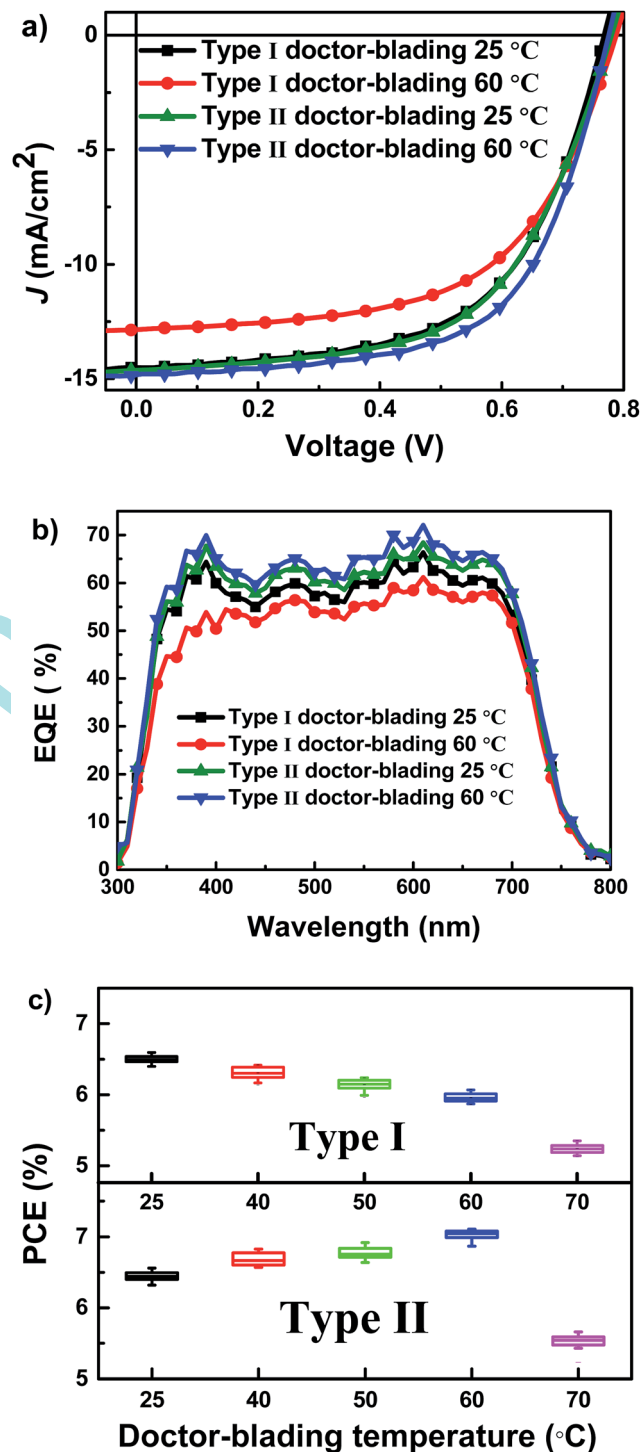


Fig. 2 (a) *J*-*V*, (b) EQE curves of Type I and Type II devices doctor-bladed at 25 and 60 °C substrate temperatures, respectively. (c) Statistical PCEs of Type I and Type II devices doctor-bladed at various substrate temperatures of 25, 40, 50, 60 and 70 °C.

etc. Moreover, the self-assembly multi-layer film formation process by doctor blading and the corresponding device physics mechanism behind fabrication have not been systematically investigated.

Based on the above existing problems, in this paper, we use an ITO-free R2R compatible inverted device structure to study the different doctor-blading processes with the relationship between the coating parameters and the device electrical values by a transient drying monitoring technique, surface energy, impedance spectroscopy, *etc.* It was proved that the doctor blading substrate temperature greatly affects the performance of the devices by changing the solvent drying time. For the one-step doctor-blading process a longer drying time promotes good interfacial layer formation *via* vertical self-assembly, which contributes to a higher PCE. The optimal substrate temperature for one-step doctor-blading IFIPSCs with the rigid backbone donor PTB7:PC₇₁BM:indene-C60 bisadduct (ICBA) system is 25 °C whereas it is 60 °C for two-step doctor-blading IFIPSCs, indicating that the one-step doctor-blade coating method is more energy saving. Moreover, from the results of film morphology and device impedance spectroscopy measurements, it's verified that the influence of substrate temperatures on the active layer morphology is not much more important than that on the PFN self-organization in the quaternary solute system (PFN:PTB7:PC₇₁BM:ICBA). Furthermore, for the semi-flexible chain donor poly[*N,N'*-bis(2-hexyldecyl)isoidindigo-6,6'-diyl-*alt*-3,3'-dioctyl-2,2':5',2''-terthiophene-5,5''-diyl] (P3TI):PC₇₁BM system, it shows better device performance at the substrate temperature of 40 °C other than the low temperature of 25 °C because of the greater influence of temperature on crystallinity morphology than the effective interfacial layer formation, illustrating the one-step doctor-blading method variety for industrial low-cost R2R production.

Results and discussion

In this work, the photoactive materials were based on PTB7 as the electron donor, PC₇₁BM and ICBA as the electron acceptors and PFN as the IBL, whose chemical structures are shown in Fig. 1a. Doping ICBA into PTB7:PC₇₁BM blends is for obtaining an improvement in energy level alignment which provides an extra new pathway for charge transfer from PTB7 to the PC₇₁BM:ICBA alloy in conjunction with the fine morphology.²⁰ The

working principle of doctor blading is described in Fig. 1b and film thickness can be well controlled by changing the fabrication parameters, including the solution concentration, angle of attack, the gap between the blade and the substrate temperature.^{21–23} In this study, the gap height was 20 μm with a modest 40 mm s⁻¹ doctor-blading speed and the same spin-coating active solution concentration of 25 mg mL⁻¹. For one-step doctor-blade coating IFIPSCs with a structure of Al/TiO_x/PFN:PTB7:PC₇₁BM:ICBA/PEDOT:PSS (Type I), PFN:BHJ nano-composite solution was directly doctor-bladed on top of the Al/TiO_x cathode with the PFN single layer formation *via* vertical self-assembly after drying. For two-step doctor-blade coating IFIPSCs with a structure of Al/TiO_x/PFN/PTB7:PC₇₁BM:ICBA/PEDOT:PSS (Type II), a conjugated polymer PFN interlayer was first spin-coated on top of the Al/TiO_x cathode and then the PTB7:PC₇₁BM:ICBA active solution was doctor-bladed on top of the PFN interlayer.

The different optimum substrate temperatures for Type I and Type II devices form an interesting contradiction. As shown in Fig. 2a, the substrate temperature has a completely different influence on the short circuit current density (J_{sc}) of Type I and Type II devices. The Type I device doctor-bladed at 25 °C substrate temperature exhibits a J_{sc} of 14.61 mA cm⁻² and a PCE of 6.56%. Upon increasing the substrate temperature to 60 °C, the J_{sc} and PCE of the Type I device decrease to 12.80 mA cm⁻² and 5.94% while the open circuit-voltage (V_{oc}) remains almost unaffected. In contrast, the Type II device doctor-bladed at 25 °C achieves a J_{sc} of 14.77 mA cm⁻² and a PCE of 6.62% which increase to 14.96 mA cm⁻² and 7.11% at the substrate temperature of 60 °C, respectively, as summarized in Table 1. The photovoltaic parameters of Type I devices doctor-bladed at 25 °C are very similar to those of Type II devices fabricated at 25 °C, demonstrating that the delamination of the PFN layer from BHJ composites for one-step doctor-blading devices is very effective. We note that PTB7:PC₇₁BM:ICBA devices without the PFN interfacial layer just show a low V_{oc} of 0.36 V and a low PCE of 1.39% for one-step spin-coated PSCs, indicating that PFN molecules can effectively deposit onto the surface of the cathode.¹⁷ To confirm the accuracy of the J - V measurements in Fig. 2a, the corresponding external quantum efficiency (EQE) curves of devices were plotted as shown in Fig. 2b. All of the devices show broad photo-responses in the wavelength range from 300 to 800 nm. The maxima of the EQEs reach 66%, 60%,

Table 1 Photovoltaic parameters of Type I and Type II devices with low and high substrate temperatures of 25 and 60 °C by doctor blading and by spin coating at room temperature under illumination of AM 1.5G (100 mW cm⁻²). Over 20 devices were tested for each averaged value^a

Type	Fabrication condition	J_{sc} (mA cm ⁻²)	V_{oc} (V)	FF	Thickness (nm)	PCE _{max} [PCE _{ave}] (%)
Type I	Doctor-blading 25 °C	14.61	0.78	0.59	115	6.56 [6.40]
Type I	Doctor-blading 60 °C	12.80	0.79	0.59	105	5.94 [5.82]
Type I	Spin-coating 25 °C	15.35	0.78	0.62	90	7.36 [7.24]
Type II	Doctor-blading 25 °C	14.77	0.78	0.58	110	6.62 [6.44]
Type II	Doctor-blading 60 °C	14.96	0.78	0.61	100	7.11 [7.03]
Type II	Spin-coating 25 °C	15.80	0.78	0.61	95	7.65 [7.55]

^a PCE_{max}: maximum power conversion efficiency; PCE_{ave}: average power conversion efficiency.

68% and 72% for 25 °C Type I, 60 °C Type I, 25 °C Type II and 60 °C Type II devices, respectively. No large differences are observed in the EQE profiles of Type I and Type II devices processed at 25 °C, which testifies the parity of the different doctor-blading fabrication processes. In truth, the parity also exists for the spin coating method. The spin-coated Type I device shows identical performance compared to the spin-coated Type II device at the same spinning substrate temperature of 25 °C (7.36% vs. 7.65%). Moreover, the tendency of statistical PCEs of the two types of devices doctor-bladed in a wide range of substrate temperatures from 25 to 70 °C indicates that Type I devices show the best performance at the lowest substrate temperature (25 °C) due to the finest stratification of PFN molecules from BHJ composites whereas Type II devices show the best device performance at a high substrate temperature of 60 °C due to the finest morphology, which will be discussed later. The complementary $J-V$ and photovoltaic parameters of the two types of devices doctor-bladed at different temperatures (25, 40, 50, 60 and 70 °C) are shown in Fig. S1 and Table S1,† as compared to the conventional spin-coated devices, displaying completely different tendency towards substrate temperatures. The PCE of Type II devices unexpectedly decreases to 5.66% when the substrate temperature reaches 70 °C due to the lower device fill factor (FF), which may come from the thin and inhomogeneous active layer influenced by the high substrate temperature.

To describe in more detail how temperature influences the solution thinning and BHJ film formation with/without (w/o) the PFN molecules mixing, we utilize a transient drying monitoring technique, *in situ* monitoring of the reflectance images, to track the different drying processes of the two kinds of films. As we know, film morphology is formed during the drying process, which is greatly affected by the rate of solvent evaporation and drying time.^{24–28} Fig. 3 shows the interference fringes of the Type I and Type II wet films processed from CB : DIO : CN (94 : 3 : 3, v/v) solvent by doctor blading at 25 and 60 °C, respectively. As shown in Fig. 3a and b, at the first stage (0–70 s at 25 °C vs. 0–40 s at 60 °C) of PFN:BHJ drying, there is approximately straight reflectance intensity because thick wet films are difficult to be interfered. Zhao *et al.* reported that this stage is mainly the evaporation of the volatile CB (131 °C) solvent.²⁹ It can be observed that a high interference oscillation frequency occurs in the second stage (70–500 s at 25 °C vs. 40–200 s at 60 °C) due to the evaporation of the additive solvent DIO (169 °C). After 500 s (25 °C) or 200 s (60 °C), the additive CN begins to evaporate. This stage exhibits a much slower drying rate and drying time because of the high boiling point property of CN (263 °C).³⁰ The final drying time, determined by the intersection of the curve's tangent and the straight line, is about 2717, 1229, 2704 and 1264 s for films processed at 25 (Type I), 60 (Type I), 25 (Type II) and 60 °C (Type II), respectively. The backtracking of the wet film thickness is enabled by the interference maxima and minima combined with a known final dry film thickness. The transient thickness decreases with the increase of time at different thinning rates, which are 1.4 and 3.0 nm s⁻¹ in the DIO evaporation phase and 0.2 and 0.42 nm s⁻¹ in the CN evaporation phase at 25 and 60 °C for Type I films,

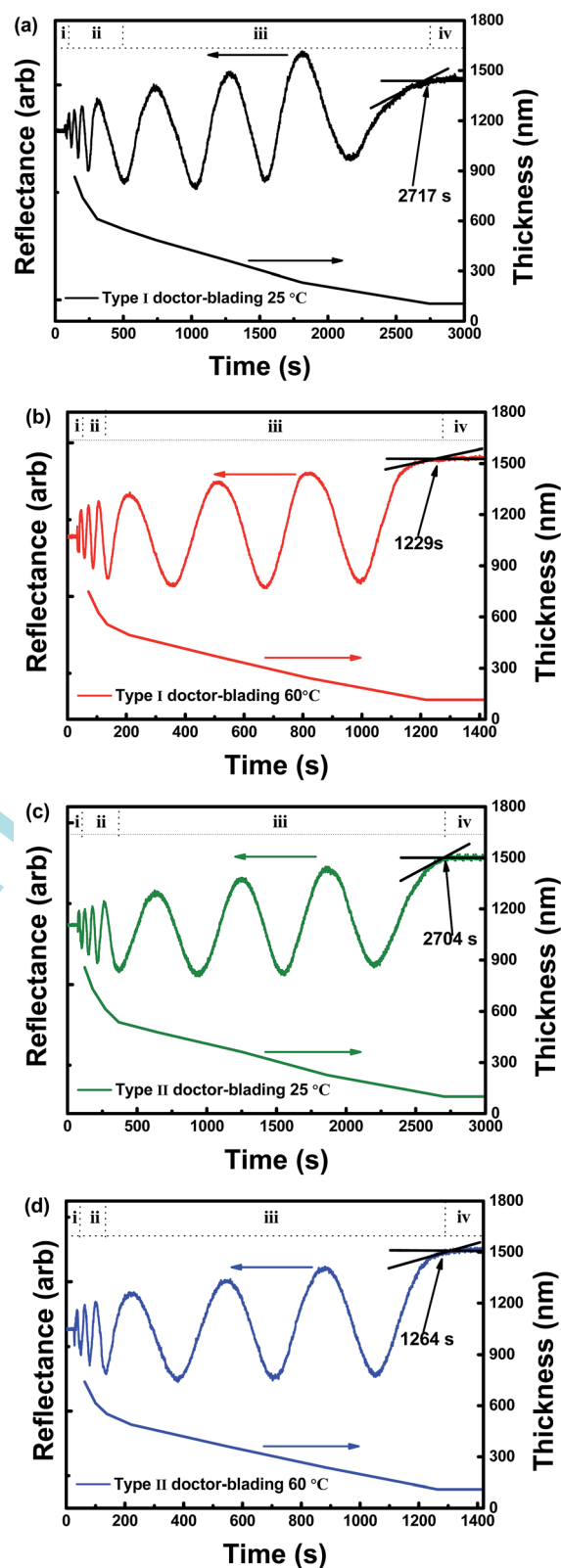


Fig. 3 The drying processes of Type I films (a) at 25 and (b) 60 °C doctor-blading substrate temperatures in comparison to those of Type II films at (c) 25 and (d) 60 °C doctor-blading substrate temperatures.

respectively. In comparison, the thinning rates are 1.3 and 2.8 nm s⁻¹ in the DIO evaporation phase and 0.19 and 0.43 nm s⁻¹ in the CN evaporation phase at 25 and 60 °C for Type II films, respectively. The mixing of tiny PFN molecules into BHJ blends seems to have no influence on the film drying process.

It was reported that different solvent drying time can influence the final active film morphology, which determines the exciton separation efficiency.¹⁸ As shown in Fig. 4, the domain size in the atomic force microscopy (AFM) images decreases when the processing temperature increases from 25 to 60 °C for both Type I and Type II films, which is consistent with the decrease of root-mean-square roughness values (4.57 nm vs. 3.65 nm at 25 °C and 2.31 nm vs. 1.73 nm at 60 °C) of Type I and Type II films, respectively. The shorter time for solidification at the higher temperature as shown in reflectance spectra (Fig. 3) can hinder crystallization and thus form finer D/A features, as disclosed in the AFM images. This can explain why the optimum doctor-blading temperature of Type II devices was achieved at 60 °C.³¹ However, Type I devices show better performance at 25 °C because of the better delamination of PFN, although AFM image shows worse morphology compared to that at 60 °C as shown in Fig. 4a and b. To get an insight into the domain sizes of the bulk films, stereoscopic topographies of the active layers were examined by transmission electron microscopy (TEM). In Fig. 4e and g, the TEM images of the BHJ and PFN:BHJ films doctor-bladed at 25 °C display bigger domains compared to those of films doctor-bladed at 60 °C (Fig. 4f and h). A clear correlation between the Type II film morphology and Type II device performance has been observed, *viz.*, films with smaller phase separations give higher performances in devices. This is because the smaller domain sizes are beneficial for excitons to diffuse to the D/A interface and sequentially dissociate into electrons and holes, resulting in reduced germinate charge recombination. However, for Type I films, although the TEM image at 60 °C shows better morphology compared to that at 25 °C, the worse PFN

delamination at the higher temperature influences device performance much stronger than the formed smaller domain sizes, which will be discussed in the later part. Thus it can be seen that the two different doctor blading processes have different requirements to favor the effective vertical delamination of the interfacial buffer layer or the finer D/A interface of the active blend layer.

It has been demonstrated that IBL self-organization is influenced by the blend composition and substrate surface energy.^{32–35} In order to perceive the effect of the substrate temperature on the stratification of PFN, the surface molecular distributions of the pristine BHJ and PFN:BHJ films were analyzed by measuring their physicochemical properties. As seen in Fig. 5a, the formamide droplet has the smallest contact angle of 65° on the spin-coated PFN film surface, whereas it is 80° for the spin-coated hydrophobic BHJ film. The similar formamide contact angle of 80° for Type I and Type II films doctor-bladed at 25 °C indicates that the surface molecular distributions do not change with different coating methods and a small amount of PFN with polar functional groups may sink to the bottom of the BHJ film during the doctor-blade coating process, resulting in the superior device performance as shown in Fig. 2 and Table 1. However, the contact angle unexpectedly decreases to 75° when the doctor-blading substrate temperature increases to 60 °C for Type I film, which mainly comes from the incomplete vertical migration of PFN molecules caused by fast solvent drying (Fig. 3), leading to the inferior device performance. It was believed that the vertical self-assembly is formed by differing surface energies in organic blends on the basis of the minimization of the total system energy.^{33,36–38} For exploring the vertical self-organization of PFN, surface energies of PFN, BHJ and PFN (3 wt%):BHJ solid films were measured based on Owens equation $\gamma_1(1 + \cos \theta) = 2(\gamma_s^D \gamma_1^D)^{1/2} + 2(\gamma_s^P \gamma_1^P)^{1/2}$, where γ_s and γ_1 are the surface energies of the sample and the probe liquid, and D and P refer to the dispersion and polar components of the surface energy, respectively (see details in Table S2

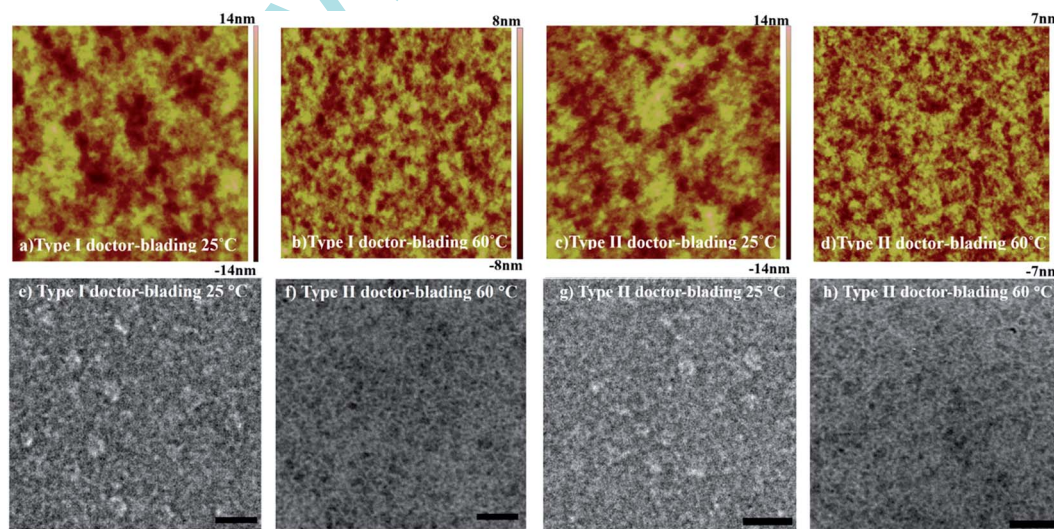


Fig. 4 AFM and TEM images of Type I films doctor-bladed at 25 °C (a and e) and 60 °C (b and f) in comparison to those of Type II films doctor-bladed at 25 °C (c and g) and 60 °C (d and h) (AFM image size: 5 μm \times 5 μm , TEM bar = 100 nm).

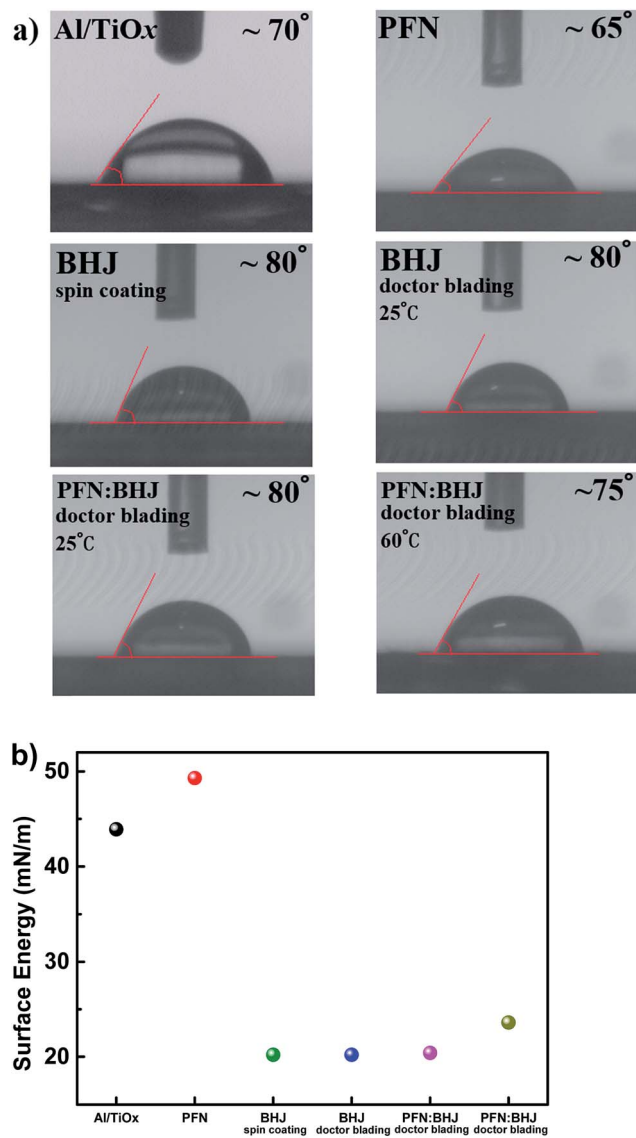


Fig. 5 (a) Photographs of formamide contact angle on top of the various films. (b) Surface energies of various films.

and S3⁺).³⁹ As displayed in Fig. 5b, the high-surface energies of PFN (49.8 mN m⁻¹) and Al/TiO_x (44.2 mN m⁻¹) indicate that PFN molecules in PFN:BHJ nanocomposites can migrate vertically towards the high-surface energy Al/TiO_x interface to

achieve a bulk free energy minimization and thus an ultrathin PFN layer can be formed thermodynamically between Al/TiO_x and the BHJ layer during the doctor-blade coating process. In other words, because the surface energy of PFN is substantially higher than that of BHJ, the buried Al/TiO_x interface would be almost exclusively composed of PFN by means of interaction free energies of the film constituents after drying. Moreover, it is important to note that the spin-coated or doctor-bladed BHJ film at 25 °C has a similar low surface energy (20.2 mN m⁻¹) to that of the doctor-bladed 3 wt% PFN:BHJ (20.4 mN m⁻¹) nanocomposite film at 25 °C, confirming that there is nearly no hydrophilic PFN molecule existing on the surface of the PFN:BHJ nanocomposite film. Upon further increasing the substrate temperature to 60 °C, the surface energy increases correspondingly from 20.4 mN m⁻¹ to 23.6 mN m⁻¹ because a small amount of PFN remains on the active layer surface. These results are in accordance with the tendency that Type I devices doctor-bladed at lower temperatures display better performances in spite of their worse morphologies as shown in Table 1 and Fig. 4.

For confirming the vertical migration of PFN molecules to the Al/TiO_x surface *via* self-assembly, the cross-sectional scanning electron microscopy (SEM) images of the two kinds of devices were measured as shown in Fig. 6. It is clear that the cross-sectional SEM image of Type I device doctor-bladed at 25 °C is quite similar to that of the Type II device at 25 °C in which the PFN layer was spin-coated independently, illustrating that PFN molecules were successfully migrated and stratified *via* self-assembly after drying for a long time. For comparison, there is still a part of the PFN molecules remaining in the BHJ of Type I device doctor-bladed at the high substrate temperature of 60 °C (Fig. 6b), leading to the lowest device performance. The observations from the SEM images conform well to the results of contact angle and surface energies in Fig. 5 and strongly demonstrate that doctor-blading substrate temperature has a significant effect on the self-assembly of PFN molecules.

To further study the reason for the enhancement of photovoltaic performance influenced by the electrical properties of the formed PFN interfaces, IFIPSCs were analyzed using impedance spectroscopy (IS).^{40–42} According to the device structure, a circuit model is defined as shown in Fig. 7a. R_0 corresponds to the electrode resistance including Al/TiO_x and PEDOT:PSS. R_1 and C_1 of the parallel connection correspond to the bulk resistance and capacitance of the BHJ layer. R_2 and C_2 of the parallel connection correspond to those of the formed

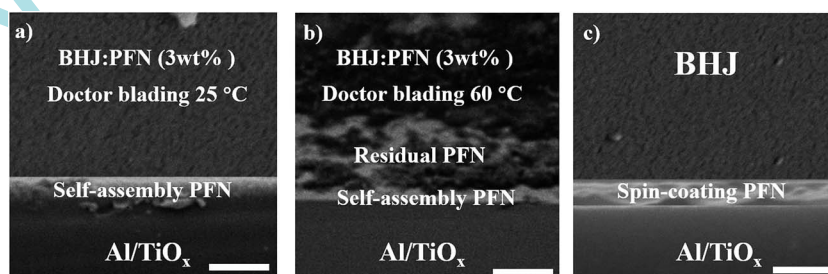


Fig. 6 Cross-sectional SEM images of (a) Type I device at 25 °C, (b) Type I device at 60 °C and (c) Type II device at 25 °C (SEM bar = 50 nm).

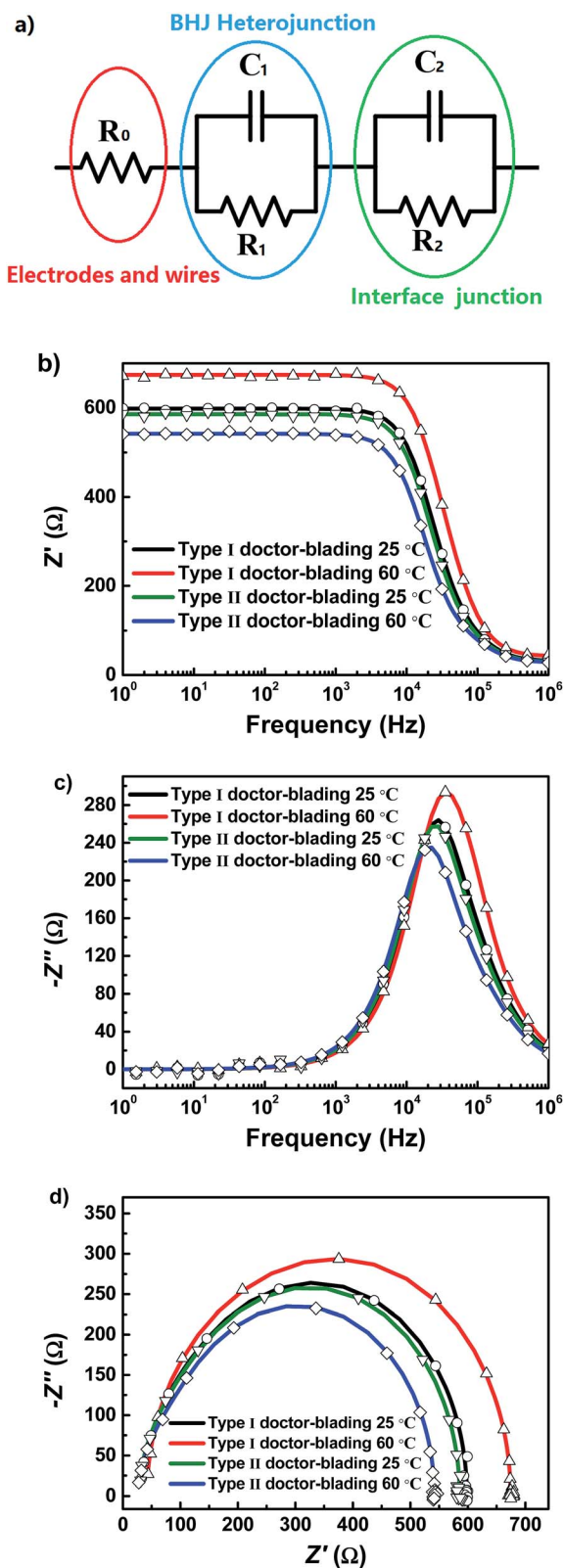


Fig. 7 The equivalent circuit model (a) of the devices and the resistance–frequency (b), reactance–frequency (c), and Cole–Cole plots (d) of Type I and Type II devices at 25 and 60 °C doctor-blading temperatures.

PFN interface layer.^{43–46} The solid lines in Fig. 7b–d are fitting based on the equivalent circuit model from experimental data. The impedance (Z) of the equivalent circuit can be expressed as the following equation.

$$Z = Z' + iZ'' = R_0 + (1/R_1 + i\omega C_1)^{-1} + (1/R_2 + i\omega C_2)^{-1} = R_0 + R_1 / (R_1^2 \omega^2 C_1^2 + 1) + R_2 / (R_2^2 \omega^2 C_2^2 + 1) - i[(R_1^2 \omega C_1) / (R_1^2 \omega^2 C_1^2 + 1) + (R_2^2 \omega C_2) / (R_2^2 \omega^2 C_2^2 + 1)]. \quad (1)$$

As shown in Fig. 7b, the resistance (Z') in the low frequency range is about 674, 598, 585 and 541 Ω for Type I (60 °C), Type I (25 °C), Type II (25 °C) and Type II (60 °C) devices, respectively, indicating the worse delamination of the PFN layer for Type I devices and the better film morphology for Type II devices at the higher substrate temperature.⁴⁷ Fig. 7c shows the reactance (Z'') vs. frequency characteristic curves, where there is only one mid-frequency peak (f_{mid}) in the test frequency range. It can be seen that f_{mid} decreases for doctor-bladed devices of Type I (60 °C), Type I (25 °C), Type II (25 °C) and Type II (60 °C) sequentially, which means that the electron lifetime is elongated and J_{sc} can be increased.^{48,49} Fig. 7d shows the combined curves of the resistance vs. corresponding reactance at different frequencies, which is also called the Cole–Cole plot. By fitting the Cole–Cole plot based on the equivalent model, each element value is obtained as listed in Table 2. R_1 decreases when the substrate temperature increases from 25 to 60 °C, illustrating the finer D/A phase separation.^{47,50} R_2 of the Type I device doctor-bladed at 60 °C is almost three times higher than other devices, indicating the bad PFN delamination in this case. It can also be seen that R_2 of the doctor-bladed self-assembly PFN formed at 25 °C is similar to that of the spin-coated pure PFN interfacial layer. Furthermore, the carrier transition time of this equivalent circuit can be calculated from the following equation:

$$C_1 = \tau_{\text{avg}} / R_1. \quad (2)$$

where τ_{avg} is the average of the carrier transition time. A longer τ_{avg} means lower carrier recombination to reach the electrodes.⁴⁵ τ_{avg} of Type I device doctor-bladed at 60 °C is shortest in all devices although the BHJ shows better morphology and lower R_1 value than that doctor-bladed at 25 °C, confirming that the performance of one-step IFIPSCs with the PTB7 donor system is primarily influenced by the inherent interfacial buffer layer stratification other than the photoactive D/A phase separation. However, if the PFN layer is pure, the better active morphology will endow τ of the Type II device with a longer lifetime.

Laser beam induced current (LBIC) maps provide valuable insight into the spatial and local distribution of photocurrent, which contributes to determining whether the loss is occurring uniformly over the sample or locally in the case of pinhole formation or other reasons.^{51,52} We find that the observed variations in film morphologies and device characteristics are corroborated by measurements with the LBIC technique under 405 nm laser beam illumination, as shown in Fig. 8. For Type I devices, the smaller intensity and more nonuniform

Table 2 IS results of Type I and Type II devices at 25 and 60 °C doctor-blading temperatures

Type	Condition	R_0 (Ω)	R_1 (Ω)	C_1 (F)	R_2 (Ω)	C_2 (F)	τ (s)
Type I	Doctor blading 25 °C	30.98	501.5	1.11×10^{-8}	65.69	1.91×10^{-8}	6.07×10^{-6}
Type I	Doctor blading 60 °C	41.89	461.4	1.15×10^{-8}	170.8	1.25×10^{-8}	5.30×10^{-6}
Type II	Doctor blading 25 °C	28.76	494.4	1.33×10^{-8}	62.44	1.95×10^{-8}	6.58×10^{-6}
Type II	Doctor blading 60 °C	27.76	453.9	2.05×10^{-8}	59.81	1.98×10^{-8}	8.03×10^{-6}

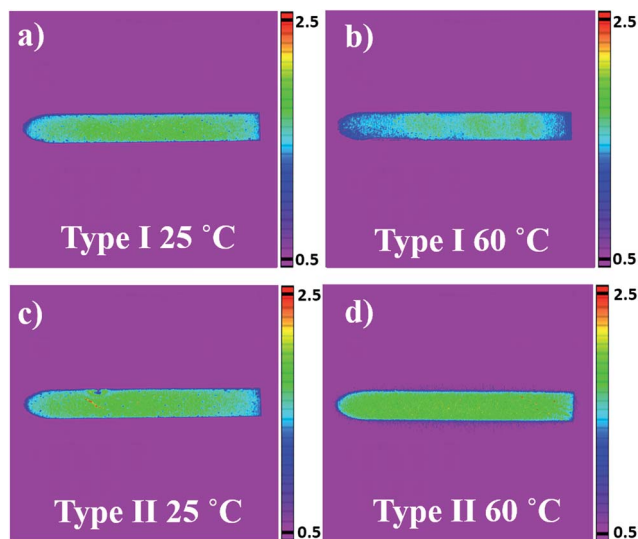


Fig. 8 LBIC images of Type I devices doctor-bladed at 25 °C (a) and 60 °C (b) in comparison to those of Type II devices at 25 °C (c) and 60 °C (d) (image dimensions: 8 mm \times 8 mm).

distribution of J_{sc} at 60 °C than at 25 °C confirm the incomplete vertical migration of PFN molecules caused by the high substrate temperature as discussed in surface energies and cross-sectional SEM images (Fig. 8a and b). In contrast, for Type II devices the cell doctor-bladed at 60 °C shows better device performance compared to that at 25 °C when the PFN layer was independently spin-coated (Fig. 8c and d), which is in accordance with the AFM and TEM results that higher temperature can hinder crystallization and thus form a finer D/A feature. Moreover, the similar LBIC images in Fig. 8a and c demonstrate that the self-assembly PFN layer doctor-bladed at 25 °C has similar properties to the spin-coated pure PFN interfacial layer.

PTB7, as one of the modern donor systems, exhibits a rigid backbone as studied herein.^{53,54} As was mentioned above, PTB7-based Type I device performance is primarily influenced by the inherent IBL stratification instead of the photoactive film morphology. For comparison, we also systematically studied one-step doctor-blading devices by replacing the PTB7 donor system with a semi-flexible P3TI system processed from 25 to 60 °C substrate temperature to discover the difference. It has been demonstrated that P3TI is a highly crystalline polymer like the classical donor polymer P3HT.^{18,55} As shown in Table S4 and Fig. S2,[†] the optimum substrate temperature for the P3TI donor system in CB:CN is 40 °C, whereas it is 25 °C for the PTB7 donor system, originating from the big influence of substrate temperatures on the active layer morphology other than the

delamination of the PFN layer. Therefore, the different donor systems should be dealt with each case on its merits for the one-step doctor-blading technique.

Conclusions

In this work, efficient ITO-free R2R compatible inverted PSCs were successfully fabricated with the combination of a self-organization method and doctor blading technology. The optimal one-step doctor-blade processed device performance was obtained at 25 °C with a PCE of 6.56%, which is similar to the optimal two-step device doctor-bladed at 60 °C with a PCE of 7.11%. Two-step devices show better performance at higher substrate temperatures due to the better active layer morphology originating from the fast solvent drying. The opposite tendency in one-step doctor-blading devices compared to two-step doctor-blading devices is that the better device performance was achieved at the low substrate temperature because integrity of the pure PFN layer is much more important than the finer D/A phase separation morphology. By analyzing the electrical information in the BHJ and PFN interface through IS measurements, the detailed reason for photovoltaic performance enhancement in these devices is confirmed. Furthermore, for highly crystalline donor polymers, BHJ morphology seems to play a bigger role in improving the doctor-bladed device performance than that in the homogeneous donor polymer. The study provides an easy-to-use route in energy-saving and low-cost PSC industrialization.

Experimental section

Materials

PTB7 and PC₇₁BM were purchased from 1-Material Inc. and Solenne Inc., respectively. PEDOT:PSS (Clevios PH1000) solution was mixed with 5% dimethyl sulfoxide (DMSO) (Alfa Aesar 99.9%) and 0.5% surfactant (FS-30) for higher conductivity and better surface wettability. The PFN, P3TI and ICBA materials were synthesized in our laboratory. PFN was dissolved in methanol (with a few drops of acetic acid to ionize PFN) with a concentration of 1 mg mL⁻¹ for spin-coating on top of the glass substrate, while PFN was dissolved in CB : DIO : CN (94 : 3 : 3 by volume) solution with a concentration of 25 mg mL⁻¹ for mixing with PTB7:PC₇₁BM:ICBA active solution. For PTB7:PC₇₁BM:ICBA active solution, the blending ratio of PTB7 : PC₇₁BM : ICBA was 1 : 1.5 : 0.25 with a concentration of 25 mg mL⁻¹ in a ternary solvent system CB : DIO : CN (94 : 3 : 3 by volume). For PFN:PTB7:PC₇₁BM:ICBA nanocomposite solution, 3 wt% of PFN from CB:DIO:CN solution with

a concentration of 25 mg mL^{-1} was doped into the PTB7:PC₇₁BM:ICBA active solution. For PFN:P3TI:PC₇₁BM solution, 3 wt% of PFN from CB:CN solution with a concentration of 20 mg mL^{-1} was doped into the P3TI:PC₇₁BM active solution with a concentration of 25 mg mL^{-1} in a binary solvent system CB : CN (97 : 3 by volume).

Device fabrication

The glass substrates were cleaned with acetone, alkaline lotion, deionized water and isopropanol in that order. For the reference two-step coating device with the inverted structure of Al/TiO_x/PFN/PTB7:PC₇₁BM:ICBA/PEDOT:PSS, 100 nm Al and 4 nm Ti were thermally evaporated under a pressure of 3×10^{-4} Pa onto the glass substrates, respectively, and exposed to air for 12 hours to form the Al/TiO_x cathode. A 10 nm thick PFN layer was first spin-coated from methanol at 2000 rpm on top of the clean glass substrate and then a PTB7:PC₇₁BM:ICBA BHJ active layer was spin-coated or doctor-bladed on top of the PFN layer. In this study, the substrate temperature was varied from 25 to 70 °C. The gap height of the doctor blade was 20 μm with a 40 mm s⁻¹ blading speed. For one-step coating devices with the inverted structure of Al/TiO_x/PFN:PTB7:PC₇₁BM:ICBA (or PFN:P3TI:PC₇₁BM)/PEDOT:PSS, active solution was spin-coated or doctor-bladed directly on top of the Al/TiO_x cathode. Finally modified PEDOT:PSS (100 nm) was spin-coated on top of the active layer.

Measurements and characterization

The current *J-V* characteristics were measured using a Keithley 2400 source meter under illumination of an AM 1.5G solar simulator with an intensity of 100 mW cm^{-2} (Sun 2000 Solar Simulator, Abet Technologies, Inc.). Contact angles using water and formamide as the testing liquids were determined on top of the solid active films using a drop shape analyzer DSA100 instrument. The EQE data were recorded with a QE-R test system from Enli Technology Company (Taiwan). The film thickness was measured by using a surface profiler (XP-2). To monitor the transient wet film drying process, a blue LED was used with its emission peak at 470 nm and a full width at half maximum (FWHM) of 22 nm, and the film specular reflection was recorded using a CMOS camera (IDS μEye). The film topography was investigated using AFM (CSPM5500) and TEM (PHILIPS TECNAI-10). The cross-sectional image was measured by SEM (ULTRA55, Zeiss). The LBIC was imaged using a pulsed laser-diode beam at 405 nm that scanned the cell's surface with an image resolution of 50 μm (LSD4). The impedance spectroscopy was performed using an electrochemical workstation (Princeton Applied Research) with an AC amplitude of 10 mV and a frequency range between 100 kHz and 1 Hz. The measured IS results were obtained at an applied bias of 0.8 V at 25 °C.

Acknowledgements

The authors are grateful to the NSFC Project (61274062, 11204106 and 11304045), the Open Fund of the State Key Laboratory of Luminescent Materials and Devices (South China

University of Technology #2012-skllmd-10) and the Fundamental Research Funds for the Central Universities for financial support. EW acknowledges the Swedish Research Council (VR) and the Excellent Doctoral Dissertations of Guangdong Province (ybzzxm201114) for financial support.

Notes and references

- 1 D. Angmo and F. C. Krebs, *J. Appl. Polym. Sci.*, 2013, **129**, 1–14.
- 2 G. Li, R. Zhu and Y. Yang, *Nat. Photonics*, 2012, **6**, 153–161.
- 3 Z. He, C. Zhong, X. Huang, W.-Y. Wong, H. Wu, L. Chen, S. Su and Y. Cao, *Adv. Mater.*, 2011, **23**, 4636–4643.
- 4 K. Xiong, L. T. Hou, P. Wang, Y. X. Xia, D. C. Chen and B. Xiao, *J. Lumin.*, 2014, **151**, 193–196.
- 5 F. C. Krebs, *Sol. Energy Mater. Sol. Cells*, 2009, **93**, 1636–1641.
- 6 F. C. Krebs, *Sol. Energy Mater. Sol. Cells*, 2009, **93**, 465–475.
- 7 S. H. Liao, H. J. Jhuo, P. N. Yeh, Y. S. Cheng, Y. L. Li, Y. H. Lee, S. Sharma and S. A. Chen, *Sci. Rep.*, 2014, **4**, 6813.
- 8 J.-D. Chen, C. Cui, Y.-Q. Li, L. Zhou, Q.-D. Ou, C. Li, Y. Li and J.-X. Tang, *Adv. Mater.*, 2015, **27**, 1035–1041.
- 9 B. Kan, M. Li, Q. Zhang, F. Liu, X. Wan, Y. Wang, W. Ni, G. Long, X. Yang, H. Feng, Y. Zuo, M. Zhang, F. Huang, Y. Cao, T. P. Russell and Y. Chen, *J. Am. Chem. Soc.*, 2015, **137**, 3886–3893.
- 10 A. Teichler, J. Perelaer, F. Kretschmer, M. D. Hager and U. S. Schubert, *Macromol. Chem. Phys.*, 2013, **214**, 664–672.
- 11 N. Li and C. J. Brabec, *Energy Environ. Sci.*, 2015, **8**, 2902–2909.
- 12 Y. Xia, K. Sun and J. Ouyang, *Adv. Mater.*, 2012, **24**, 2436–2440.
- 13 M. Jørgensen, K. Norrman and F. C. Krebs, *Sol. Energy Mater. Sol. Cells*, 2008, **92**, 686–714.
- 14 Z. Tang, L. M. Andersson, Z. George, K. Vandewal, K. Tvingstedt, P. Heriksson, R. Kroon, M. R. Andersson and O. Inganäs, *Adv. Mater.*, 2012, **24**, 554.
- 15 M. Manceau, D. Angmo, M. Jørgensen and F. C. Krebs, *Org. Electron.*, 2011, **12**, 566–574.
- 16 T. Ji, L. Tan, J. Bai, X. Hu, S. Xiao and Y. Chen, *Carbon*, 2016, **98**, 15–23.
- 17 Z. Peng, Y. Zhang, Y. Xia, K. Xiong, C. Cai, L. Xia, Z. Hu, K. Zhang, F. Huang and L. Hou, *J. Mater. Chem. A*, 2015, **3**, 20500–20507.
- 18 K. Xiong, L. T. Hou, M. X. Wu, Y. C. Huo, W. S. Mo, Y. F. Yuan, S. Sun, W. Xu and E. G. Wang, *Sol. Energy Mater. Sol. Cells*, 2015, **132**, 252–259.
- 19 H. Zhang, W.-Y. Tan, S. Fladischer, L. Ke, T. Ameri, N. Li, M. Turbiez, E. Spiecker, X.-H. Zhu, Y. Cao and C. J. Brabec, *J. Mater. Chem. A*, 2016, **4**, 5032–5038.
- 20 Z. Peng, Y. Xia, F. Gao, K. Xiong, Z. Hu, D. I. James, J. Chen, E. Wang and L. Hou, *J. Mater. Chem. A*, 2015, **3**, 18365–18371.
- 21 Y. H. Chang, S. R. Tseng, C. Y. Chen, H. F. Meng, E. C. Chen, S. F. Horng and C. S. Hsu, *Org. Electron.*, 2009, **10**, 741–746.
- 22 R. Mens, F. Demir, G. Van Assche, B. Van Mele, D. Vanderzande and P. Adriaensens, *J. Polym. Sci., Part A: Polym. Chem.*, 2012, **50**, 1037–1041.

- 23 L. Wengeler, M. Schmitt, K. Peters, P. Scharfer and W. Schabel, *Chem. Eng. Process.*, 2013, **68**, 38–44.
- 24 L. T. Hou, E. Wang, J. Bergqvist, B. V. Andersson, Z. Q. Wang, C. Muller, M. Campoy-Quiles, M. R. Andersson, F. L. Zhang and O. Inganäs, *Adv. Funct. Mater.*, 2011, **21**, 3169–3175.
- 25 M. T. Dang, G. Wantz, H. Bejbouji, M. Urien, O. J. Dautel, L. Vignau and L. Hirsch, *Sol. Energy Mater. Sol. Cells*, 2011, **95**, 3408–3418.
- 26 B. Schmidt-Hansberg, M. Sanyal, M. F. G. Klein, M. Pfaff, N. Schnabel, S. Jaiser, A. Vorobiev, E. Müller, A. Colsmann, P. Scharfer, D. Gerthsen, U. Lemmer, E. Barrena and W. Schabel, *ACS Nano*, 2011, **5**, 8579–8590.
- 27 T. Wang, A. D. F. Dunbar, P. A. Staniec, A. J. Pearson, P. E. Hopkinson, J. E. MacDonald, S. Lilliu, C. Pizzey, N. J. Terrill, A. M. Donald, A. J. Ryan, R. A. L. Jones and D. G. Lidzey, *Soft Matter*, 2010, **6**, 4128–4134.
- 28 J. Yuan, L. Qiu, Z. Zhang, Y. Li, Y. He, L. Jiang and Y. Zou, *Chem. Commun.*, 2016, **52**, 6881.
- 29 K. Zhao, H. Hu, E. Spada, L. K. Jagadamma, B. Yan, M. Abdelsamie, Y. Yang, L. Yu, R. Munir, R. Li, G. O. N. Ndjawa and A. Amassian, *J. Mater. Chem. A*, 2016, **4**, 16036–16046.
- 30 J. Bergqvist, S. A. Mauger, K. Tvingstedt, H. Arwin and O. Inganäs, *Sol. Energy Mater. Sol. Cells*, 2013, **114**, 89–98.
- 31 J. Yuan, L. Qiu, Z.-G. Zhang, Y. Li, Y. Chen and Y. Zou, *Nano Energy*, 2016, **30**, 312.
- 32 T. Ameri, P. Khoram, T. Heumüller, D. Baran, F. Machui, A. Troeger, V. Sgobba, D. M. Guldi, M. Halik and S. Rathgeber, *J. Mater. Chem. A*, 2014, **2**, 19461–19472.
- 33 K. Yao, L. Chen, X. Chen and Y. Chen, *Chem. Mater.*, 2013, **25**, 897–904.
- 34 D. Ma, M. Lv, M. Lei, J. Zhu, H. Wang and X. Chen, *ACS Nano*, 2014, **8**, 1601–1608.
- 35 A.-C. Baudouin, J. Devaux and C. Bailly, *Polymer*, 2010, **51**, 1341–1354.
- 36 H. Kang, S. Kee, K. Yu, J. Lee, G. Kim, J. Kim, J. R. Kim, J. Kong and K. Lee, *Adv. Mater.*, 2015, **27**, 1408–1413.
- 37 P. Fu, L. Huang, W. Yu, D. Yang, G. Liu, L. Zhou, J. Zhang and C. Li, *Nano Energy*, 2015, **13**, 275–282.
- 38 Q. Wei, T. Nishizawa, K. Tajima and K. Hashimoto, *Adv. Mater.*, 2008, **20**, 2211–2216.
- 39 D. K. Owens and R. Wendt, *J. Appl. Polym. Sci.*, 1969, **13**, 1741–1747.
- 40 W. L. Leong, S. R. Cowan and A. J. Heeger, *Adv. Energy Mater.*, 2011, **1**, 517–522.
- 41 Z. a. Tan, C. Yang, E. Zhou, X. Wang and Y. Li, *Appl. Phys. Lett.*, 2007, **91**, 023509.
- 42 S.-M. Park and J.-S. Yoo, *Anal. Chem.*, 2003, **75**, 455–A.
- 43 K. Hess, *Advanced Theory of Semiconductor Devices*, Wiley-IEEE Press, 2000.
- 44 J. Bisquert, *Phys. Chem. Chem. Phys.*, 2003, **5**, 5360.
- 45 E.-P. Yao, C.-C. Chen, J. Gao, Y. Liu, Q. Chen, M. Cai, W.-C. Hsu, Z. Hong, G. Li and Y. Yang, *Sol. Energy Mater. Sol. Cells*, 2014, **130**, 20–26.
- 46 S. Yum, T. K. An, X. Wang, W. Lee, M. A. Uddin, Y. J. Kim, T. L. Nguyen, S. Xu, S. Hwang, C. E. Park and H. Y. Woo, *Chem. Mater.*, 2014, **26**, 2147–2154.
- 47 W. Xu, R. Xia, T. Ye, L. Zhao, Z. Kan, Y. Mei, C. Yan, X.-W. Zhang, W.-Y. Lai, P. E. Keivanidis and W. Huang, *Adv. Sci.*, 2016, **3**, 2198–3844.
- 48 J. Xia, L. Chen and S. Yanagida, *J. Mater. Chem.*, 2011, **21**, 4644.
- 49 Q. Wang, J.-E. Moser and M. Grätzel, *J. Phys. Chem. B*, 2005, **109**, 14945–14953.
- 50 W. Huang, J. Peng, L. Wang, J. Wang and Y. Cao, *Appl. Phys. Lett.*, 2008, **92**, 013308.
- 51 C. H. Peters, I. T. Sachs-Quintana, J. P. Kastrop, S. Beaupré, M. Leclerc and M. D. McGehee, *Adv. Energy Mater.*, 2011, **1**, 491–494.
- 52 F. C. Krebs, R. Søndergaard and M. Jørgensen, *Sol. Energy Mater. Sol. Cells*, 2011, **95**, 1348–1353.
- 53 L. Lu and L. Yu, *Adv. Mater.*, 2014, **26**, 4413–4430.
- 54 Y. Liang, Z. Xu, J. Xia, S. T. Tsai, Y. Wu, G. Li, C. Ray and L. Yu, *Adv. Mater.*, 2010, **22**, 135–138.
- 55 Z. F. Ma, W. J. Sun, S. Himmelberger, K. Vandewal, Z. Tang, J. Bergqvist, A. Salleo, J. W. Andreasen, O. Inganäs, M. R. Andersson, C. Muller, F. L. Zhang and E. R. Wang, *Energy Environ. Sci.*, 2014, **7**, 361–369.